SPACEDUST-Optical: Wide-FOV Space Situational Awareness from Orbit

Randa Qashoa
York University
Matthew Driedger[a], Ryan Clark[b], Paul Harrison[a], Michael Berezin[a], Regina Lee[c], Andrew Howarth[d]
[a]Magellan Aerospace, [b]C-CORE, [c]York University, [d]University of Calgary

ABSTRACT

This paper presents the SPACEDUST-Optical prototype; an end-to-end space situational awareness system that includes RSO prediction, detection, identification, and orbit refinement. The system uses wide field of view (FOV) images from spacecraft such as CASSIOPE's Fast Auroral Imager camera or star trackers for RSO detection but is designed to be imager-agnostic to leverage many orbital imaging platforms. The system expands our understanding of the space environment by utilizing operational space assets to observe RSOs, increasing the number of RSO detections and better-refining RSO orbit estimates for these detected RSOs, using existing operational orbital sensors such as wide FOV cameras and star trackers.

1. INTRODUCTION

The proliferation of resident space objects (RSOs) in the near-Earth realm requires increased monitoring capabilities to ensure the safety and security of space-based infrastructure. Ground-based systems, using both radar and narrow field optical systems, currently form the backbone of this monitoring-and-follow-up capability, supported by space-based surveillance missions. However, space-based platforms have the potential to vastly increase coverage of LEO orbital regimes, being unaffected by weather or geographic considerations, but their implementations tend to be optimized for GEO, MEO, and HEO object tracking.

This paper presents the solutions for LEO object detection that Magellan Aerospace and its collaborators at York University, C-CORE, and the University of Calgary have been developing since 2017. With funding from Canada's Department of National Defence, Magellan and its partners are implementing this prototype system as part of a project called SPACEDUST (Special Processes and Advanced Computing Environment for Detection, Unambiguity, Surveying, and Tracking). The SPACEDUST-Optical prototype uses images from space-based cameras, such as the CASSIOPE satellite's Fast Auroral Imager (FAI) [1], to perform the full cycle of RSO prediction, detection, identification, and refinement.

While the Optical Prototype is designed to use imagery from a variety of sensors, FAI images are especially well suited for demonstrating the Optical Prototype's performance. The FAI camera's FOV and detection capability are analogous to those of star trackers, and its images contain many RSOs of interest, especially in polar regions that are difficult to access by ground systems. Although small in aperture, star trackers are ideal for background sky object monitoring due to their wide fields-of-view (FOV) of ~20° across or more [2]. Additionally, their coarse pixel resolution reduces signal loss from streaking due to high relative angular rates in LEO. The real potential of these commercial-off-the-shelf (COTS) sensors, however, is their ubiquity – star trackers are currently employed by hundreds of spacecraft for attitude determination [3]. If dual-purposed for RSO monitoring, the collective coverage offered by these "backyard orbiting observatories" in LEO would be immense.

The prototype system presented in this paper regularly images RSOs of interest by first predicting RSO access times, simulating RSO images to confirm if the RSOs in question will likely be visible, imaging these RSOs using the FAI camera, detecting RSOs in the resulting images, and then identifying the detected RSOs. Section 2 provides details on the prototype design while Section 3 presents the results of validating the prototype. These results are discussed in Section 4 while Section 5 concludes the paper.

2. PROTOTYPE DESIGN

The SPACEDUST Component 1b Optical Prototype is a technology demonstrator for detecting and identifying RSOs within images taken by space-borne optical instruments. The Optical prototype includes two functional modes: Active-Search Mode and Passive Search Mode. Active-Search Mode forecasts when RSOs may enter a space-borne optical

instrument's FOV, sends imaging requests to spacecraft operators for these access periods, and proceeds to perform object detection, identification, and orbital refinement on the resulting images. The Passive-Search Mode searches for RSOs in existing images from available image databases and performs object identification and orbital refinement on any detected RSOs within these images. These two modes, including their subcomponents, are shown in Fig. 1 and Fig. 2.

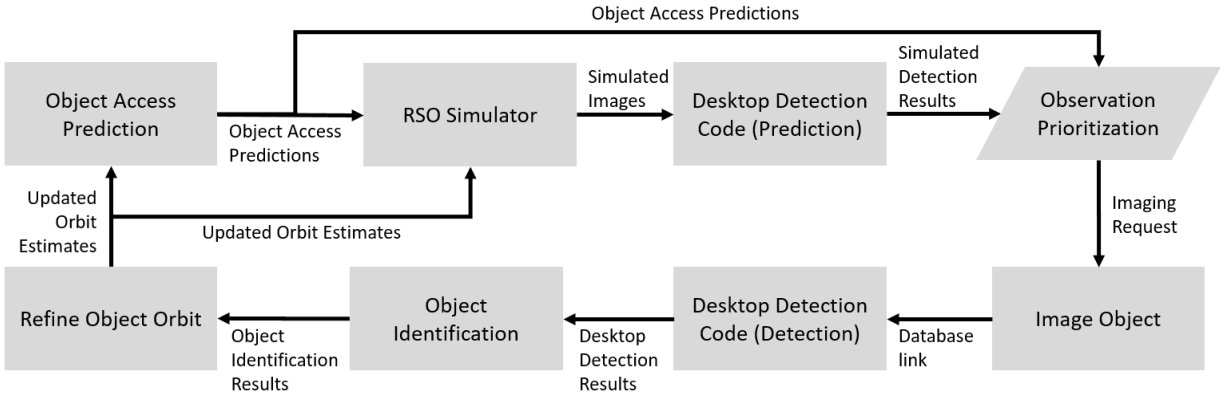

Fig. 1. SPACEDUST Optical Prototype Active Mode

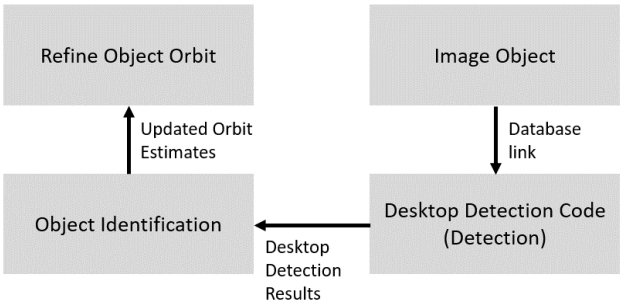

Fig. 2. SPACEDUST Optical Prototype Passive Mode

The Optical Prototype is designed to use multiple participating space-based optical sensors. However, for testing and demonstration purposes, the prototype uses a combination of real and simulated images from the FAI optical camera onboard the CASSIOPE spacecraft [1] for RSO detection and identification.

The remainder of this section provides details on each of the SPACEDUST Optical Prototype's constituent parts.

2.1 RSO ACCESS PREDICTION

To know when to schedule imaging requests with an orbital imaging platform, such as FAI, a prediction tool is needed in order to determine when an RSO is going to be in the camera's FOV. The developed prediction tool uses the desired target objects' TLEs, the host's TLE, timing information, sensor parameters, and pointing information to simulate the target object's position in the sensor's FOV and provide user with the access times and locations for each target object. The access prediction tool leverages advances in modern day hardware and parallel processing to execute these simulations. Currently, the tool uses sensor and orbital parameters for FAI to predict when RSOs of interest will pass through FAI's FOV. Fig. 3 presents a block diagram of the access prediction tool.

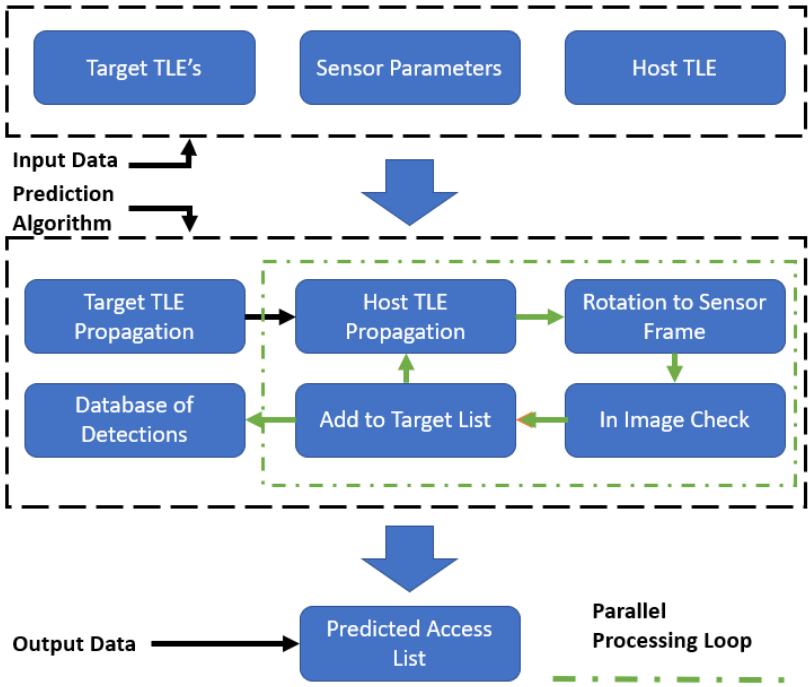

Fig. 3. Block diagram of the RSO Prediction Tool

2.2 RSO IMAGE SIMULATION

To better validate if the RSOs determined from the RSO prediction list are in view of FAI, we used a starfield optical image simulator, called the Space Based Optical Image Simulator (SBOIS), that generates simulated images from the FOV of a specified observer. SBOIS was originally designed as part of a study to assess whether star trackers can be feasibly used for RSO imaging. More details on the simulator's basic functionality are provided in [4]. Since then, the simulator has been updated with many new features such as ground-based mode, tracking mode, and most recently, an anti-sun pointing mode.

To generate a simulated image from a specified host RSO, its ephemeris file or TLE and an attitude profile needs to be provided as an input to SBOIS, alongside the TLEs of potential targets and the host RSO's sensor parameter information. Given that the RSO simulations are performed before the RSO is imaged onboard CASSIOPE, we cannot provide ephemeris files and the RSO's attitude needs to be estimated. Since FAI is currently locked in an anti-sun pointing configuration [5], an anti-sun pointing mode option was implemented within the simulator for this study. This should provide an appropriate attitude estimate to approximate FAI's pointing profile while using TLEs to calculate RSO positions and velocities. Since the prediction list generated by the Optical Prototype's RSO Access Prediction algorithm already performs the first step of identifying potential targets, SBOIS has been modified to only simulate these potential target RSOs rather than simulating the full RSO catalog. Additionally, the prediction list allows us to limit the simulation time so as to only simulate images during the predicted access window, along with a predefined buffer time simulated before and after this window to account for potential errors in propagating the target and host RSOs.

To implement anti-sun pointing mode, the sun vector in the host RSO's body frame needs to be determined. Following that, the vector is flipped such that it points in anti-sun direction. We then convert the anti-sun vector to the host RSO's orbit frame and calculate the yaw, pitch, and roll needed to point the host RSO in the anti-sun direction. Once the host RSO's attitude has been calculated, the simulator uses the prediction list to determine which RSOs are in view of the observer and generates a simulated image and a .mat file describing details of the target such as position, velocity, and pixel entry and exit locations.

2.3 RSO DETECTION

The Optical Prototype's RSO Detection function predicts the centroids and brightness of any RSOs present in a provided image set and matches RSO detections between images to the same parent object, following the process shown in Fig. 4. To detect these RSOs, the function first pre-processes rolling sets of 3 images to remove background noise, hot pixels, and stars. Removing these features from the images aids the neural network and reduces false positives. The three lit pixel lists are then converted into a single RGB image, with each colour channel representing one of the three original images, to enable processing by a Faster Recurrent Convolutional Neural Network (Faster R-CNN) [6]. Finally, a Gaussian convolution is applied to the combined image to magnify the features within the image. The processed image is passed to the Faster R-CNN which creates a bounding box surrounding each suspected RSO and an associated confidence score between 0 and 1. The centroids and estimated brightness of each detected object are extracted and objects that persist between frames are matched to the same parent object. Finally, the brightness values, centroid locations, parent object IDs, and other telemetry are saved to a .csv file for further analysis.

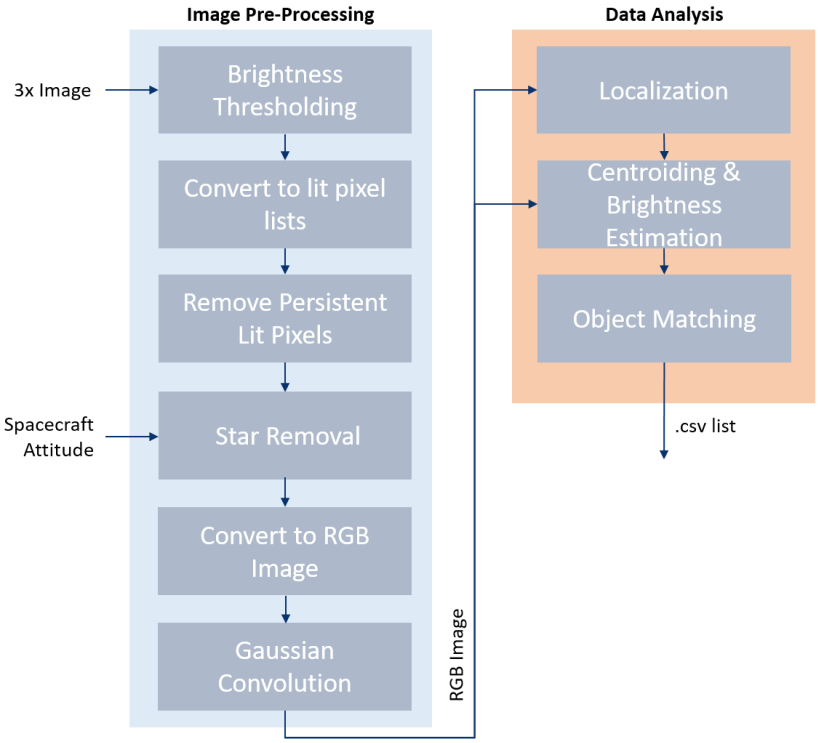

Fig. 4. RSO Detection

The remainder of this subsection describes each of the RSO Detection function's features in further detail.

Image Pre-Processing

Image pre-processing first thresholds rolling sets of 3 images to remove background noise by subtracting a fixed value from each pixel. The images are then converted to lit pixel lists and these lists are compared to each other to identify and remove any persistent lit pixels between the images. While the persistent lit pixel removal algorithm is capable of removing hot pixels caused by radiation effects, this algorithm will not remove any stars from the images if the imaging spacecraft is rotating, as is the case for CASSIOPE. From our preliminary development of the Optical Prototype, we found that stars were a major source of false positives and that a star removal algorithm was necessary to improve the prototype's performance.

To determine the star's apparent movement on the camera's image plane, we approximated the camera as a pin-hole camera and used the camera matrix to relate an object's position in a three dimensional camera-centred Cartesian coordinate frame X to the object's position in the camera's two dimensional image plane x [7]:

$$\lambda x = PX \tag{1}$$

where λ is the distance from the camera's focal plane to the object and P is the camera matrix. P has two components: the intrinsic matrix K, which is a function of the camera's physical parameters, and the extrinsic matrix $[R\ |t]$ which is a function of the camera's position and orientation. The intrinsic matrix K is expressed as:

$$K = \begin{bmatrix} f & s & W/2 \\ 0 & f & H/2 \\ 0 & 0 & 1 \end{bmatrix} \quad (2)$$

where f is the focal length, W is the image plane width, H is the image plane height, and s is the image skew. Generally, for image sensors with square pixels, s can be assumed to be 0. The extrinsic matrix is expressed as [7]:

$$[R|t] = \begin{bmatrix} r_{1,1} & r_{1,2} & r_{1,3} & t_1 \\ r_{2,1} & r_{2,2} & r_{2,3} & t_2 \\ r_{3,1} & r_{3,2} & r_{3,3} & t_3 \\ 0 & 0 & 0 & 1 \end{bmatrix} \quad (3)$$

The final row makes the matrix square and allows the matrix to be simplified to a rotation R followed by a translation t [7]:

$$[R|t] = [I \mid t] * \begin{bmatrix} R & 0 \\ 0 & 1 \end{bmatrix} \quad (4)$$

where t is a 3x1 matrix containing the camera's translation in x, y, and z axes respectively and R is a 3x3 rotation matrix. Together, the camera matrix P is [7]:

$$P = \begin{bmatrix} f & s & W/2 \\ 0 & f & H/2 \\ 0 & 0 & 1 \end{bmatrix} [I \mid t] * \begin{bmatrix} R & 0 \\ 0 & 1 \end{bmatrix} \quad (5)$$

To predict the expected apparent movement of a fixed object, such as a star, from one frame to the next due to the camera's rotation, we expressed the star's position in the image plane x_o at an initial timestep t_0 and at a subsequent timestep t_1. At timestep t_0, the star's position in the image plane can be expressed using Equation (1) as:

$$\lambda x_0 = P_o X \quad (6)$$

and at t_1 as:

$$\lambda x_1 = P_1 X \quad (7)$$

Note that P_0 is not a square matrix and so we used theorem 5.1.7 from [8] to express the star's position in the three dimensional frame X as a function of x_0. This Theorem states that the minimum solution x_{min} for a matrix A that is n x m sized, with $n < m$ and $rank(A) = n$ is:

$$Ax = b \ \rightarrow \ x_{min} = A^T (AA^T)^{-1} b \quad \text{Theorem 1}$$

applying this to Equation (6),

$$\lambda x_0 {P_o}^T \left(P_o {P_o}^T\right)^{-1} = X \quad (6b)$$

and combining Equation (6b) with Equation (7), we found the star's new apparent position as a function of the camera matrices and the star's initial position in the image plane:

$$\lambda x_1 = \lambda x_0 P_1 {P_o}^T \left(P_o {P_o}^T\right)^{-1} \quad (8)$$

Which can be simplified to:

$$x_1 = x_0 P_1 {P_o}^T \left(P_o {P_o}^T\right)^{-1} \quad (9)$$

Assuming that the camera is at the centre of the camera's reference frame, pointing along the frame, P_0 can be simplified to

$$P_0 = \begin{bmatrix} f & s & W/2 \\ 0 & f & H/2 \\ 0 & 0 & 1 \end{bmatrix} \begin{bmatrix} 1 & 0 & 0 & 0 \\ 0 & 1 & 0 & 0 \\ 0 & 0 & 1 & 0 \end{bmatrix} \begin{bmatrix} 1 & 0 & 0 & 0 \\ 0 & 1 & 0 & 0 \\ 0 & 0 & 1 & 0 \\ 0 & 0 & 0 & 1 \end{bmatrix} = \begin{bmatrix} f & 0 & W/2 & 0 \\ 0 & f & H/2 & 0 \\ 0 & 0 & 1 & 0 \end{bmatrix} \quad (10)$$

This means we only have to consider the small angle change between the two images. With this assumption, neglecting the camera's translation between images, and using the Euler 321 rotation sequence, P_1 becomes

$$P_1 = \begin{bmatrix} f & s & W/2 \\ 0 & f & H/2 \\ 0 & 0 & 1 \end{bmatrix} \begin{bmatrix} 1 & 0 & 0 & 0 \\ 0 & 1 & 0 & 0 \\ 0 & 0 & 1 & 0 \end{bmatrix} \begin{bmatrix} c2c3 & c2s3 & -s2 & 0 \\ -c1s3 + s1s2c3 & c1c3 + s1s2s3 & s1c2 & 0 \\ s1s3 + c1s2c3 & -s1c3 + c1s2s3 & c1c2 & 0 \\ 0 & 0 & 0 & 1 \end{bmatrix} = \begin{bmatrix} f & s & W/2 \\ 0 & f & H/2 \\ 0 & 0 & 1 \end{bmatrix} \begin{bmatrix} c2c3 & c2s3 & -s2 & 0 \\ -c1s3 + s1s2c3 & c1c3 + s1s2s3 & s1c2 & 0 \\ s1s3 + c1s2c3 & -s1c3 + c1s2s3 & c1c2 & 0 \\ 0 & 0 & 0 & 1 \end{bmatrix} \quad (11)$$

Note that due to the small expected change in attitude between images, we are unlikely to run into gimbal lock when using Euler angles. The assumption that the camera will not translate between images is not strictly valid, as at orbital speeds the camera is travelling at several kilometers per second. However, when imaging fixed stars that are light-years away from the camera, the relative change in star distance is negligible and the zero-translation approximation holds.

By applying the initial camera matrix P_0 and final camera matrix P_1, as defined in Equations (9) and (10), to Equation (8), we calculated the predicted motion of each object between image frames. Any objects located in these predicted locations in the subsequent frame were assumed to be stars and removed.

Localization, Centroiding, and Brightness Estimation

Pre-processed images were fed into a custom-trained Faster R-CNN [6]. While this neural network is no longer state of the art, Faster R-CNN has fewer layers and learnable parameters than more recent networks such as the YOLO series [9], which are designed to detect significantly more complex features than the stars and RSOs present in star tracker and FAI images. The neural network was trained using a set of 214 hand-labelled processed FAI images and was validated using a second set of 75 hand-labelled processed FAI images.

The Faster R-CNN provides bounding box coordinates as well as a confidence scores between 0 and 1 for each predicted RSO. Any predictions with scores below 0.8 are discarded and the Optical Prototype calculates the centroid and average brightness for each remaining RSO prediction. Using these bounding boxes, the Optical Prototype calculates the centroid and average brightness for each RSO prediction. Centroids are calculated using the Centre of Gravity algorithm [10] while brightness is calculated as the mean pixel intensity of all pixels greater than the average pixel intensity within the bounding box.

Object Matching

Once any RSOs within a set of images have been identified and centroided, the Optical Prototype uses a Hough Transform [11] to match sightings of the same object between images to the same parent object. The Hough Transform draws a series of lines at different angles θ which intersect with each centroid. The Hough Transform then calculates the minimum distance r between each line and the frame origin. Any objects that fall along the same line will have approximately the same minimum radius r for a given angle θ. Fig. 5 shows an example of the Hough Transform matching two objects, A and B. Three lines were drawn centred on Object A and centred on Object B at angles θ_1, θ_2, and θ_3. The corresponding minimum distances r were calculated, and the line between Object A and Object B was found by determining the angle θ_2 where the minimum distance r_2 is most similar between the two objects.

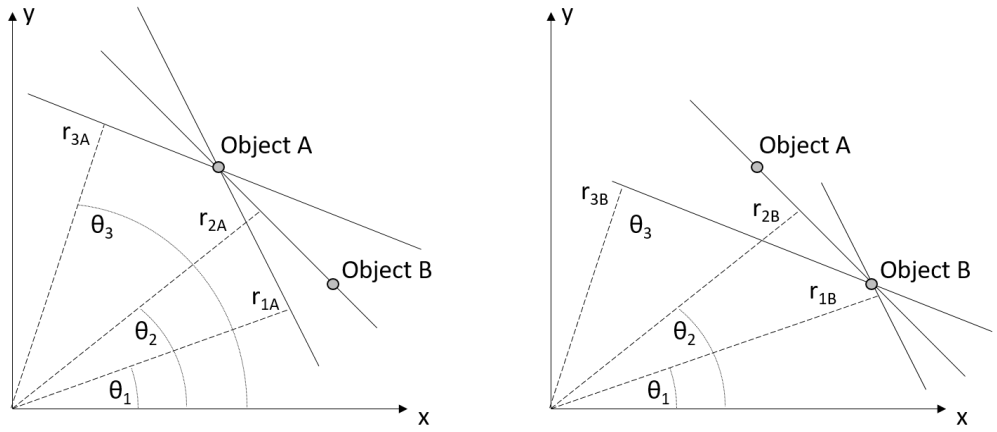

Fig. 5. Hough Transform Example

While the above example demonstrates how the Hough Transform functions graphically, computationally r is calculated for a given centroid with coordinates x and y at a given angle θ as:

$$r = x\cos(\theta) + y\sin(\theta) \tag{12}$$

However, the process of finding the line between each object using r is the same as previously described. Using the Hough Transform, we calculated r for angles θ between 0° and 180° for each RSO detection in a rolling set of 5 images. If 3 or more detections in this rolling set of images shared the same r for the same angle θ, within a 4° tolerance, they were assigned to the same parent RSO ID. Any object detected four or more times across the image set was passed onto the RSO Identification algorithm to determine the object's catalog number.

2.4 RSO IDENTIFICATION

When the detector algorithm identifies an object passing through the image sequence, the subsequent identification algorithm determines which RSO the object represents. This identification process factors in timing, host position, velocity, sensor data, and the pixel location of the RSO in relation to the timing. The RSO's identification hinges on an objective function that incorporates multiple factors, as delineated in Equation (13). For the identification to be deemed accurate, the object's score from the objective function should not only be the lowest among all candidates but also possess a confidence value of at least 4. This confidence metric is derived by dividing the score of the top candidate by the score of the runner-up, indicating how much better the leading candidate's score is compared to the second-best.

$$Score = Pos * Cur(1 + Distance) \tag{13}$$

Pos is the average position accuracy of the RSO, Cur is the curve accuracy of the RSO, and $Distance$ is the distance factor.

The average position accuracy measures the deviation between the predicted and observed positions of a target RSO. In the early stages of this research, we only considered the entry and exit points of an object within a sequence. However, this approach identified numerous potential candidates corresponding to the observed positions. By evaluating the entire sequence, we significantly reduced the number of candidate objects. The average position error for a sequence is determined using Equation (14), with its constituent variables elaborated upon subsequently.

$$POS = \frac{\sum \sqrt{\left(X_m - X_p\right)^2 + \left(Y_m - Y_p\right)^2}}{n} \tag{14}$$

X_m is the measured centroid X pixel, X_p is the predicted centroid X pixel, Y_m is the measured centroid Y pixel, Y_p is the predicted centroid Y pixel, and n is the total number of points used.

The curve accuracy quantifies the discrepancies in coefficients when modeling the object's trajectory across the sequence with a cubic function. The inclusion of a cubic path function addresses biases arising from discrepancies between the actual and predicted positions in the TLE. Though there might be positional offsets, the relative trajectory, which also captures effects from the host satellite (like positional shifts and attitude adjustments), often remains consistent. Incorporating curve accuracy helps counteract this offset error by augmenting it with the relative path.

To ascertain the curve error, we first fit a curve to both the tracked object's trajectory over the sequence and all target RSOs. We then compute the relative difference between each coefficient, excluding the 0th order, and sum these differences to yield the curve accuracy score, as detailed in Equation (15).

$$Cur = \sum \frac{\left|Coef_{meas,n} - Coef_{pre,n}\right|}{Coef_{meas,n}} \quad 15$$

$Coef_{meas,n}$ is the calculated coefficient of order *n* from the measured path and $Coef_{pre,n}$ is the calculated coefficient of order *n* from the predicted path.

The last factor that was included was the distance factor. During preliminary testing, we observed that RSOs, considerably outside the camera's FOV, were occasionally flagged as potential identification candidates. To rectify this, we introduced the distance factor. Though the present implementation seems effective, it is worth noting that a more sophisticated approach—perhaps one that leverages both distance and size to ascertain relative brightness—might further increase the confidence in our results. Equation (16) shows the distance factor calculation:

$$Dis = \frac{r_{predicted}}{2{,}500} \quad 16$$

where $r_{predicted}$ is the absolute distance between the potential RSO and host in kilometers.

2.5 RSO ORBIT REFINEMENT

After correlating an object and its trajectory to a NORAD ID, using our RSO Identification method, we refine the object's orbit using the short ARC pass and Initial Orbital Determination (IOD). One inherent challenge with angle-only space-based measurements is the range degeneracy issue. This complexity emerges when attempting to estimate three positional points using only two measurement points, namely the pixel location. To address this, we augmented the measurements of known objects with pseudo-ranges derived from the known objects' TLE. Our IOD methodology follows the approach detailed in [12], leveraging the pseudo-ranges provided by the object's TLE for the initial range estimates.

3. TESTING

The following section describes the tests that we have performed to verify the performance of the various elements of the SPACEDUST Optical Prototype.

RSO Access Prediction

Testing the access prediction algorithm requires a dataset containing detections of known objects. Currently, we are preparing this dataset by passing FAI image sequences through our RSO detection and identification algorithms. Once a sufficient number of FAI images containing known RSOs with available ephemeris data have been gathered, we will begin formally testing the access prediction tool.

RSO Image Simulation

To test the RSO simulator, we created identical scenarios using the RSO simulator and using Systems Tool Kit's (STK's) Electro-Optical & Infrared (EOIR) sensors tool, which is typically used in the industry for RSO image simulations. Then, we compared the results of these scenarios to determine whether the same RSO appears in both simulation tools within a similar time window. Out of 22 sequences determined from the RSO access prediction list, 21 of them were predicted by the simulator, and 20 were predicted by STK-EOIR. There was one sequence from the

prediction list that did not appear in either the RSO simulator or STK-EOIR and there was one sequence that was visible in the RSO simulator but not visible in STK-EOIR. These discrepancies could have been due to propagation errors which caused the RSOs to appear outside the simulation window that we examined.

For all the common sequences, the RSO entry and exit times were compared between the RSO simulator and STK-EOIR as shown in Fig. 5.

(a) Start-time difference (b) End-time difference

Fig. 6. Difference in RSO entry and exit times between the RSO simulator and STK-EOIR.

From Fig. 5, we can see that the difference in starts times did not exceed 9 seconds. When predicting the end times of a sequence, the differences increased to a maximum of 100 seconds. However, most differences in sequence end time values were below 20 seconds.

RSO Detection

We conducted preliminary testing of the Optical Prototype's RSO detection algorithm using a set of 332 labelled FAI images. These FAI images resulted in a rolling set of 330 RGB images once they were pre-processed by the detection algorithm. Fig. 7 shows an example of the predicted RSO locations provided by the detector's Faster R-CNN and the resulting matched RSO detections generated using the Hough Transform. Despite the efforts that we made in pre-processing the FAI images, some stars remained in the processed image due to small errors in CASSIOPE's attitude estimate. These remaining stars, as well as noise sources such as lens flair, resulted in false-positive RSO detections. Fig. 7 exhibits one such false positive, caused by an un-removed star. Although not the case for this example, the Hough Transform was able to remove the majority of these false positives. The detection algorithm had a 73.6% true positive rate and a 32.1% recall rate, meaning that 73.6% of the algorithm's predicted RSO locations corresponded to actual RSOs and that the algorithm identified 32.1% of all RSOs within the image set. While these results are not unreasonable, false positives increase the processing requirements for the overall Optical Prototype, as the RSO identification algorithm must attempt to match these nonexistant RSOs to objects in the RSO catalogue. Conversely, false negatives represent missed opportunities to better understand the orbital behaviour of these undetected RSOs. As such, improving the detection algorithm's performance will be one of our major goals moving forward.

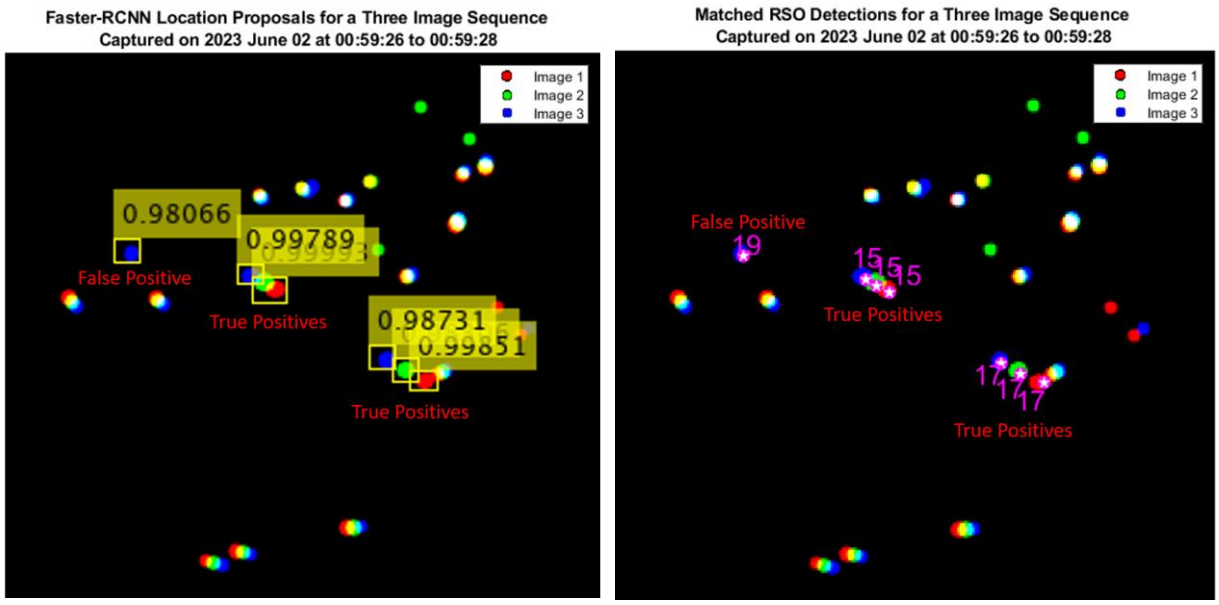

Fig. 7. Faster R-CNN Detection Results before (left) and after (right) the Hough Transform was applied

RSO Identification

To validate the accuracy of the RSO identification tool, we require image sequences of objects with either known ephemeris data or recognized configurations. Using the identification algorithm, we have been able to identify different bright RSO's such as RCM, Starlink, and ONEWEB satellites in FAI images. Our initial assessments focused on sequences capturing RCM shortly after its launch, during which time the satellites maintained a formation. This arrangement expedited manual object identification. Such sequences have been elaborated upon in [4]. During these preliminary evaluations, our algorithm successfully identified RCM satellites from the unclassified NORAD catalog in 5 out of the 6 sequences. In the remaining sequence, while the RCM satellites were recognized, the tool struggled to differentiate between RCM 1 and RCM 2, as the confidence value fell short of the minimum threshold of 4.

Encouraged by these initial results, we are currently examining the algorithm's efficacy in identifying Starlink detections from FAI images. Given the public availability of Starlink's ephemeris data, it will serve as a benchmark to validate our algorithm's output. We anticipate concluding our tests in the coming months. The insights gleaned will culminate in a comprehensive paper, exploring the interplay between the objective function and the identification algorithm's precision.

RSO Orbit Refinement

We applied our IOD method, based on the methodology in [12], to the Starlink detections identified by our RSO Identification algorithm, using these satellites' publicly accessible ephemeris data to verify our orbit estimates. Based on a limited sample of fewer than ten sequences, the IOD positioning reduced the error relative to the TLE by approximately 30%. While these findings are encouraging, the sample size is insufficient and lacks diversity for definitive conclusions. As we process more sequences, an increasing number become available for IOD testing. Once we have analyzed over 30 sequences and discernible patterns emerge, we will present more conclusive insights into the enhancements IOD offers for orbital refinement.

In instances where the RSO orbit refinement algorithm detects the same object multiple times in a single day, the IOD method's accuracy can be increased through data fusion. To realize this, we employed an Unscented Kalman Filter (UKF) [13] to integrate the IOD results from each sequence with the TLE data to yield a more accurate positional estimate. Preliminary trials using the UKF revealed an accuracy enhancement of roughly 50% across three test days. However, the UKF demands fine-tuning for peak efficacy and these preliminary tests used non-optimized UKF parameters. As such, the UKF may offer further accuracy improvements once we amass a sufficiently large dataset of Starlink detections with which to train and test the UKF.

4. DISCUSSION

The results presented in this paper are promising, however they are based on limited initial testing. As we continue to advance the SPACEDUST Optical Prototype, our primary focus will be on conducting more thorough tests of each of the prototype's constituent algorithms and functionally testing the prototype as a whole. Additionally, these preliminary tests allowed us to identify several areas where the prototype's performance can be improved: replacing the RSO detection algorithm's star removal method with an iterative closest point (ICP) based method; enhancing the RSO detection algorithm's RSO matching method to reduce false matches; training the detection algorithm's neural network on a larger dataset; and optimizing the orbit refinement method's UKF using an expanded dataset of Starlink detections.

While the RSO detection algorithm's star removal method was generally effective in removing stars, this method also removed slow-moving RSOs from the images and any RSOs that crossed in front of a star. Additionally, this method required accurate attitude information from the spacecraft. When the attitude estimate quality decreased, the method removed fewer stars and resulted in the Faster R-CNN generating an increased number of false positives. While attitude information is necessary for RSO identification, fine attitude estimates could be generated using the stars visible in each frame. Reducing the prototype's dependence on fine attitude estimates would improve the overall prototype's performance and enable the prototype to be used on platforms without fine pointing estimates. Due to these factors, future iterations of the Optical Prototype will transition to an ICP based star removal method.

Object matching is another area where the RSO detection algorithm must be improved. While the current Hough Transform is generally capable of matching different instances of the same RSO to each other across images, it occasionally fails to link matched-sets of the same RSO to each other or includes incorrect detections in these matched sets. Both of these faults decrease the performance of the RSO detection method by reducing the available data with which to make an estimate and by introducing significant error sources into the identification process respectively. To address these issues, we will be augmenting the Hough Transform with additional logical checks, such as using the RSO's estimated trajectory and brightness during the matching process.

The final improvement to the RSO detection algorithm will be to re-train the algorithm's Faster R-CNN neural network using an expanded training dataset. While the neural network produced reasonable location proposals when provided with low-noise FAI images, noise sources such as lens flare resulted in a significant number of false positive detections. As previously discussed, the detector's present performance is a major area for improvement and strengthing the performance of the neural network itself will be a central part of this future work.

5. CONCLUSION

This paper presented the preliminary design and testing of the SPACEDUST-Optical prototype; an end-to-end space situational awareness system for performing RSO prediction, detection, identification, and orbit refinement using wide field of view images from spacecraft such as CASSIOPE's FAI camera and star trackers. Based on our preliminary testing, all of the Optical Prototype's subcomponents are functional. The access prediction algorithm is capable of predicting access events between CASSIOPE and selected target RSOs, although verification of the access prediction algorithm is still necessary; the RSO Simulator can predict when CASSIOPE's FAI camera will detect target RSOs, with typical start and end time errors of less than 9 and 20 seconds respectively based on a simulated comparison between the RSO Simulator and STK-EOIR; the RSO detection algorithm is capable of detecting RSOs in FAI images with a true positive detection rate of 73.6% and a recall rate of 32.1%; the RSO identification algorithm can identify different bright RSO's such as Starlink, RCM, and ONEWEB satellites using FAI images; and the RSO orbit refinement method reduced the ephemeris error of detected Starlink satellites by 30% relative to TLEs, based on a limited sample set of less than ten sequences.

Our preliminary test results demonstrate the system's viability and we will continue to develop this prototype by improving the system's RSO detection algorithm, optimizing the orbit refinement algorithm's UKF, and better-quantifying the system's overall performance through further testing. As space becomes increasingly congested, systems such as the SPACEDUST-Optical prototype will become more and more critical in protecting the space environment by identifying and tracking RSOs.

6. ACKNOWLEDGEMENTS

The authors would like to thank Canada's Department of National Defense for funding this research to develop space debris detection methods, under the auspices of its Innovation for Defence Excellence and Security (IDEaS) Component 1b program.

REFERENCES

[1] L. Cogger, A. Howarth, A. Yau, A. White, G. Enno, T. Trondsen, D. Asquin, B. Gordon, P. Marchand, D. Ng, G. Burley, M. Lessard and B. Sadler, "Fast Auroral Imager (FAI) for the e-POP Mission," *Space Sci Rev,* vol. 189, pp. 15-25, 2015.

[2] S. Clemens, R. Lee, P. Harrison and W. Soh, "Feasibility of Using Commercial Star Trackers for On-Orbit Resident Space Object Detection," in *Proceedings of the Advanced Maui Optical and Space Surveillance Technologies Conference*, Maui, USA, 2018.

[3] S. Dave and R. Lee, "Feasibility of a Virtual Constellation using Small Aperture, Wide Field of View Optical Systems for Space Domain Awareness and Applications," in *Proceedings of the Advanced Maui Optical and Space Surveillance Technologies Conference*, Maui, USA, 2022.

[4] R. Clark, Y. Fu, S. Dave and R. Lee, "Simulation of RSO Images for Space Situation Awareness (SSA) Using Parallel Processing," *Sensors,* vol. 21, no. 23, 7868, 2021.

[5] "Routine CASSIOPE (Swarm-Echo) Science Operations Come to an End," [Online]. Available: https://epop.phys.ucalgary.ca/routine-cassiope-swarm-echo-science-operations-come-to-an-end/.

[6] S. Ren, K. He, R. Girshick and J. Sun, "Faster R-CNN: Towards Real-Time Object Detection with Region Proposal Networks," *Advances in Neural Information Processing Systems,* vol. 28, 2015.

[7] A. Heyden and M. Pollefeys, "Chapter 3, Multiple View Geometry," in *Emerging Topics in Computer Vision*, Hoboken, U.S, Prentice Hall PTR, 2005.

[8] K. B. Petersen and M. S. Pedersen, *The Matrix Cookbook*, Kongens Lyngby, Denmark: Technical University of Denmark, 2012.

[9] J. Terven and D. Cordova-Esparza, "A Comprehensive Review of YOLO: From YOLOv1 and Beyond," *arXiv*, 2023.

[10] R. C. Stone, "A Comparison of Digital Centering Algorithms," *Astron. J,* vol. 97, no. 4, pp. 1227-1237, 1989.

[11] R. O. Duda and P. E. Hart, "Use of the Hough Transformation to Detect Lines and Curves in Pictures," *Comm. ACM,* vol. 15, no. 1, pp. 11-15, 1972.

[12] D. A. Vallado, *Fundamentals of Astrodynamics and Applications 2nd Ed*., Berlin, Germany: Springer Science & Business Media, 2001.

[13] S. J. Julier and J. K. Uhlmann, "Unscented filtering and nonlinear estimation," *Proceedings of the IEEE,* vol. 92, no. 3, pp. 401-422, 2004.